

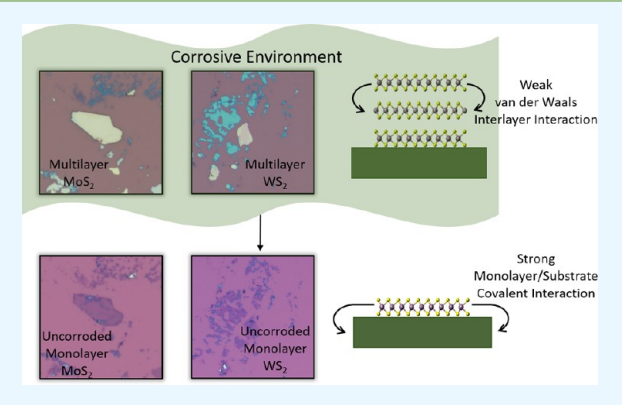
Superior Electro-Oxidation and Corrosion Resistance of Monolayer **Transition Metal Disulfides**

Daniel S. Schulman, Dan May-Rawding, Fu Zhang, Drew Buzzell, Nasim Alem, and Saptarshi Das*, \$10

[†]Materials Science and Engineering, [‡]Energy Engineering, and [§]Engineering Science and Mechanics, Pennsylvania State University, University Park, Pennsylvania 16802, United States

Supporting Information

ABSTRACT: Physics of monolayer and few-layer transition metal dichalcogenides (TMDs) and chemistry of few-layer TMDs have been well studied in recent years in the context of future electronic, optoelectronic, and energy harvesting applications. However, what has escaped the attention of the scientific community is the unique chemistry of monolayer TMDs. It has been demonstrated that the basal plane of multilayer TMDs is chemically inert, whereas edge sites are chemically active. In this article, we experimentally demonstrate that the edge reactivity of the TMDs can be significantly impeded at the monolayer limit through monolayer/substrate interaction, thus making the monolayers highly resistant to electrooxidation and corrosion. In particular, we found that fewlayer flakes of MoS2 and WS2 exfoliated on conductive TiN substrates are readily corroded beyond a certain positive electrode



potential, while monolayer remnants are left behind unscathed. The electrooxidation resistance of monolayers was confirmed using a plethora of characterization techniques including atomic force microscope (AFM) imaging, Raman spectroscopy, photoluminescence (PL) mapping, scanning/transmission electron microscope (S/TEM) imaging, and selected area electron diffraction (SAED). It is believed that strong substrate monolayer interaction compared to the relatively weak interlayer van der Waals interaction is responsible for the superior monolayers chemical stability in highly corrosive oxidizing environments. Our findings could pave the way for the implementation of monolayer transition metal disulfides as superior anticorrosion coating which can have a significant socioeconomic impact.

KEYWORDS: electrooxidation, corrosion, transition metal disulfides, monolayers, electro-ablation

INTRODUCTION

Today, corrosion is a global economic challenge affecting infrastructure, manufacturing, and consumer products. It is defined as the monotonic degradation of a precious substance and hence its properties as a result of continuous reactions with its surroundings. Fortunately, corrosion can be controlled, slowed, and even eliminated through smart material engineering. Use of corrosion inhibitors in the form of thin sacrificial coatings or platings are one of the most popular approaches toward the minimization of metallic and nonmetallic corrosion. 1-3 Development of efficient and low-cost corrosion inhibitors will have great socioeconomic impact. In this context, our finding of the extraordinary corrosion (oxidation) resistance of monolayer transition metal disulfides can be considered groundbreaking from the point of view of both fundamental corrosion chemistry of atomically thin layers and commercial implementation of monolayer materials into useful applications.

Prior to the surge of graphene publications following its discovery in 2004,4 the transition metal dichalcogenides (TMDs) were only of interest for a few niche applications. Doped and nanocomposite MoS2 found early commercial application as lubricants and coatings.⁵ However, such tribological applications that utilize MoS₂ nanoparticles in conjunction with other matrix components, although greatly reduced friction, did not offer improvements in corrosion resistance.^{6,7} In recent times, the chemistry of TMDs has mostly been focused on energy harvesting and energy storage. Nanoparticles, nanosheets, and nanotubes of MoS₂ and WS₂ have been studied as excellent catalysts for electrochemical and photoelectrochemical water splitting reactions which convert solar energy into clean hydrogen energy.⁸⁻¹⁰ It is worth mentioning that due to their superior resistance to photocorrosion, these materials also showed promise as photoanodes in photoelectrochemical cells with efficiencies exceeding 10%. 11,12 Given the layered structure with the transition metal atoms residing in octahedral or trigonal prismatic sites, TMDs are ideal systems to study intercalation of metals, Lewis

Received: November 19, 2017 Accepted: December 26, 2017 Published: December 26, 2017



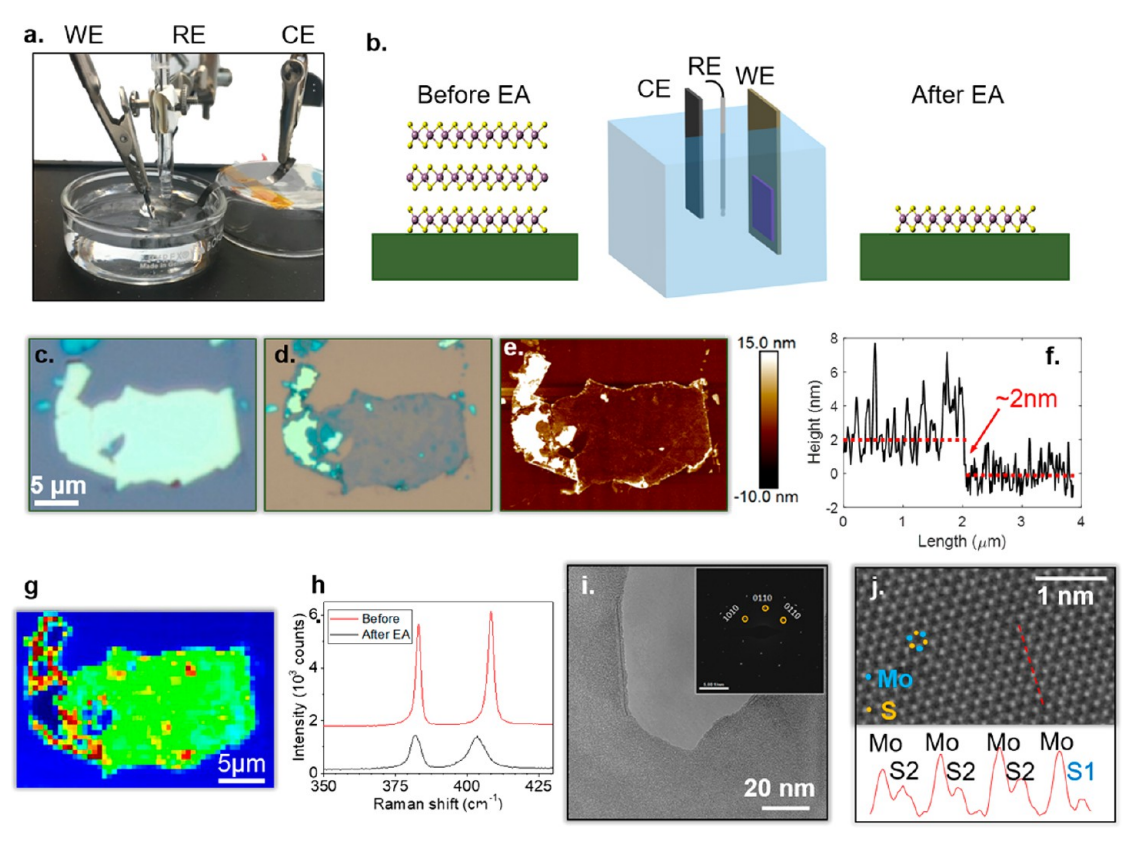


Figure 1. Electroablation process and monolayer characterization. (a) Experimental setup: the sample or the working electrode (WE) is suspended into approximately 25 mL of the electrolyte solution. A graphite counter electrode (CE) and a Ag/AgCl reference electrode (RE) are placed into the solution within a few millimeters of the WE. (b) Schematic showing the dynamics of the EA process. After application of a positive electrode potential, multilayer flakes on the 100 nm TiN coated Si substrate are converted to single layer. The flakes are etched from the edges, whereas the basal planes are unscathed. (c, d) Optical and (e) atomic force microscope (AFM) images showing mechanically exfoliated MoS₂ flake before and after 10 s EA treatment. (f) AFM line scan showing an \sim 2 nm step height after EA. (g) Photoluminescence (PL) map with submicrometer resolution showing strong PL enhancement across the entire area of the remnant flake. The intense PL observed is owed to the indirect to direct bandgap transition at the K point in the Brillouin zone in monolayers and is severely suppressed in multilayers of multilayers of MoS₂. The map color corresponds to the integrate PL peak area. (h) MoS₂ Raman spectra taken using a 488 nm laser show the E_{2g} and A_{1g} separation decreasing from 25.3 to 21.5 cm⁻¹ after flakes are converted to monolayer by the EA treatment at pH of 3 for 60 s. (i) TEM image of the MoS₂ edge showing a folded monolayer, inset SAED with hexagonal patterns indicates good crystallinity of the 2H-phase MoS₂ flake. (j) Atomic resolution annular dark field scanning TEM (ADF-STEM) image of the single layer MoS₂ distinguishing Mo and S atoms due to their Z-contrast.

bases, and organometallics which forms the basis of the next generations of supercapacitors. 13-15 This intercalation chemistry also leads to the discovery of 2H-TaS2 as a hightemperature superconductor and is now seceded by new physics which show the promise of valleytronics, straintronics, piezotronics, biotronics, and optoelectronics. 16-20 These applications exploit the noncentrosymmetry offered by monolayer TMDs such as MoS2 and WS2 but not present in multilayer TMDs or graphene. The extraordinary interaction of light with monolayers of TMDs is paving the way for the next generations of advanced optical devices such as ultrathin microlenses, gratings, resonant cavities, and waveguides. ^{21–24} In lieu of the above discussion, it is apparent that the superior electrooxidation resistance of monolayer TMDs, in particular the substrate enhanced monolayer stability presented in this work, will have paramount importance for a wide range of applications, irrespective of whether the monolayer TMD is used as an active device component or as a corrosion inhibitory sacrificial coating to the active device component. In fact, it was reported that 2D field effect transistors (FETs) based on MoS₂, WS₂, and MoSe₂ monolayers produced via the same electroablation (EA) process presented in the work maintain their

high-quality semiconducting properties comparable to materials grown via chemical vapor deposition (CVD).²⁵

Earlier studies on oxidation of bulk TMD crystals have established that the basal plane of these layered materials are chemically inert, whereas edge sites, surface steps, and dislocations are highly reactive. 26,27 However, only a handful of works have looked at the stability of TMDs at the atomistic limit.^{28–30} Castellanos-Gomez et al.³¹ recently developed a selflimiting laser-thinning process similar to our electro-ablation (EA) process³² which reduces exfoliated multilayer flakes into corresponding monolayers irrespective of their initial thicknesses. The fundamental difference between the two techniques lies in the fact that laser thinning is thermally driven, whereas electroablation is electrochemically driven. The self-limiting aspect of laser thinning is attributed to poor interlayer heat dissipation compared to the monolayer/substrate heat dissipation, whereas the self-limiting aspect of the EA process is attributed to weak interlayer van der Waals interactions compared to monolayer/substrate covalent interactions.³² Density function theory (DFT) calculations found a weak interlayer binding energy of -0.16 eV between MoS₂ layers and a much stronger binding energy of -1.25 eV between the bottom layer and TiN substrate.³² Both processes point to

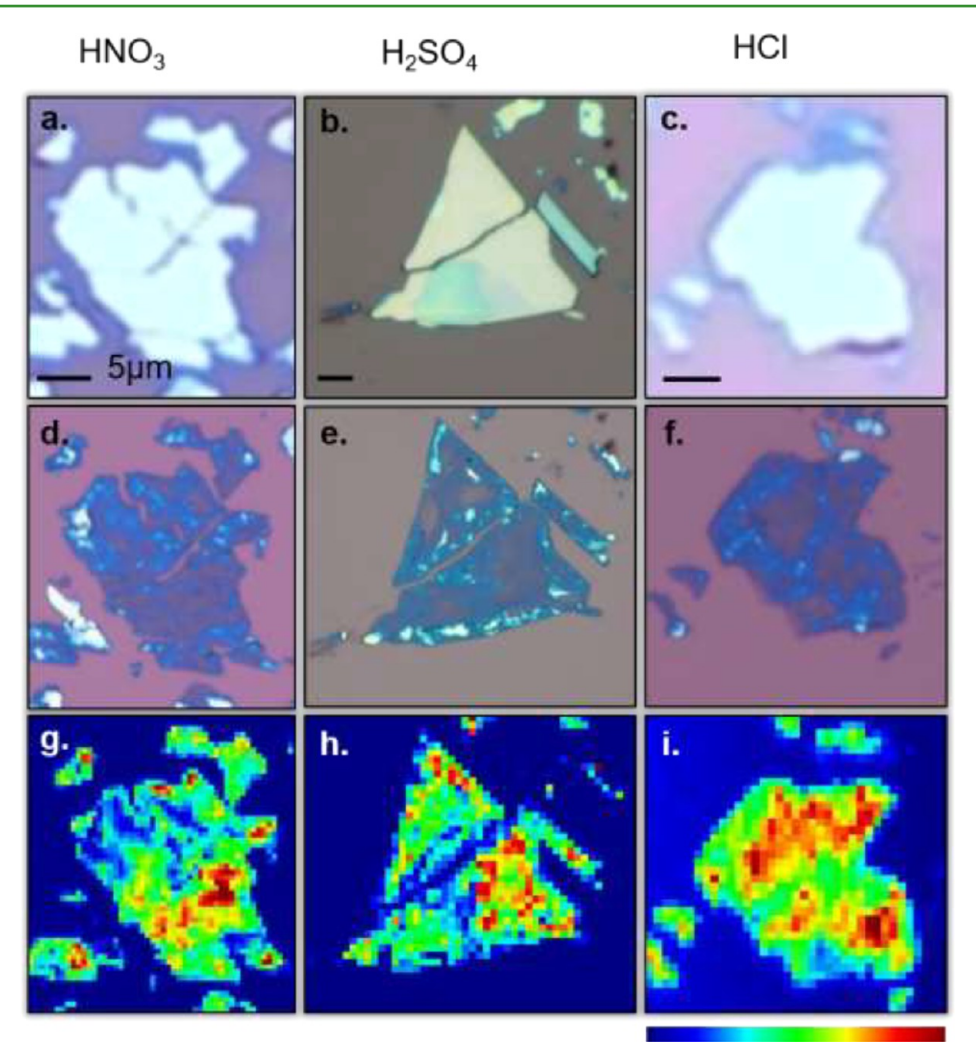


Figure 2. MoS_2 EA process in different acid electrolytes. Optical images of MoS_2 flakes (a-c) prior to and (d-f) after EA treatment for 60 s at 1.5 V in 0.1 M HNO₃, H₂SO₄, and HCl, respectively. (g-i) Photoluminescence (PL) maps for each acid after EA. The scales for the integrated PL peak area maps are consistent between each acid.

these substrate-stabilized monolayers being highly stable not only upon heating and irradiation but also in corrosive oxidizing conditions. Other reports of such self-limiting layer-by-layer oxidation, thermal sublimation, and soft plasma etching can be found in recent literature. ^{33,34} The robustness demonstrated by these TMD materials is strongly contrasted by other layered materials such as phosphorene. Phosphorene with a corrugated orthorhombic structure is highly susceptible to oxidation by ambient oxygen and water greatly reducing its feasibility as a semiconductor despite its desirable properties.³⁵ The group IV semiconducting monochalcogenides such as Ge and Sn sulfides and selenides, despite having an orthorhombic structure similar to phosphorene, are predicted to be significantly more resistant to oxidation with an activation energy for chemisorption of oxygen twice that of phosphorene. 36,37 The TMDs, with their hexagonal structure, physisorb with a remarkably low binding energy for O₂ and H₂O, only 79 and 110 meV for MoS₂, increasing to 110 and 150 meV when binding to a sulfur vacancy. Charge transfer due to this physisorption coupled with the high surface area results in dramatic changes in sheet densities but is fully reversible demonstrating the inert nature of these materials.³⁸ Both the group IV monochalcogenides and the TMDs are resistant to ambient oxygen, and even when chemisorbed onto chalcogen vacancy sites degradation of their

semiconducting properties is minimal.^{36,39} In the present work we elucidate on the chemistry of electrooxidation processes involved in the EA technique and establish the exceptional chemical stability of monolayers of transition metal disulfides compared to their bulk counterparts.

■ RESULTS AND DISCUSSION

The substrate-assisted electroablation technique for the synthesis of WS2 and MoS2 monolayer flakes was studied using conventional electrochemical voltammetry in order to better understand the monolayer stability in corrosive oxidizing environments. A plethora of characterization techniques which include atomic force microscopy (AFM), Raman spectroscopy, photoluminescence (PL) mapping, atomic resolution scanning/transmission electron microscope (S/ TEM) imaging, and selected area electron diffraction (SAED) were used to elucidate and complement our experimental findings. We also identified the threshold potential, pH dependence, electrolyte invariance, substrate composition, and topographic invariance of the EA process and hypothesized reaction species generated during the electrooxidative corrosion of multilayer TMD flakes. We also provide critical insight into the temporal evolution of the electrooxidation resistance of monolayer remnants for both MoS₂ and WS₂.

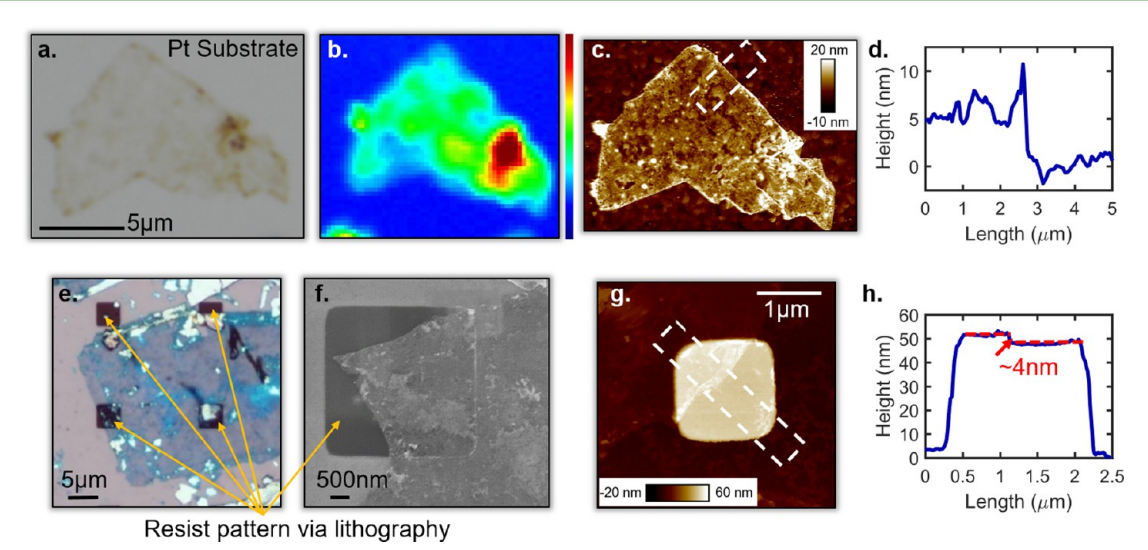


Figure 3. MoS_2 EA process on Pt and polymer substrates. (a) Optical image of monolayer MoS_2 after EA treatment for 360 s at pH = 3 and at 1.5 V on a Pt substrate. (b) Photoluminescence (PL) map showing a high PL intensity confirming the remnants are single layer MoS_2 . (c) AFM image of the flake after EA. (d) Line scan showing a step height of 5 nm consistent with monolayer step heights observed on TiN. The line scan height was averaged over a 1 μ m width due to the large substrate surface roughness. (e) Optical image and (f) SEM image of monolayer MoS_2 after EA treatment for 60 s at pH = 3 and at 1.5 V on PMGI photoresist patterned TiN. (g) AFM image and (h) height profile of the flake after EA. A 4 nm step height was measured on both the polymer and TiN regions.

Figures 1a and 1b show the experimental setup and process schematic of the EA technique, respectively. Multilayer MoS₂ and WS₂ flakes were transferred onto a 100 nm TiN coated Si substrate (used as the working electrode: WE) via mechanical exfoliation. Ag/AgCl reference electrode (RE) and a flexible graphite counter electrode (CE) were used in the electrochemical cell in order to perform the voltammogram measurements. The optical images for MoS2 flakes shown in Figures 1c and 1d demonstrate substantial change in the flake/ substrate contrast before and after the EA treatment, respectively. The AFM image and the corresponding height profile of the remnant flake are shown in Figures 1e and 1f, respectively. The flake thickness was found to be \sim 2 nm, which is greater than the expected 0.65 nm corresponding to monolayer thickness. The apparent increase in the monolayer thickness could be due to the weak etching of the underlying TiN substrate during the EA process. Another plausible explanation is that reaction products are not fully hydrolyzed into soluble species and remain on the surface, effectively increasing the thickness of the material. Nevertheless, the AFM image might not be the most convincing evidence of monolayer formation. This led to the PL map in Figure 1g with submicrometer resolution which shows strong PL enhancement across the entire area of the remnant flake. The map color corresponds to the integrated PL peak area. The intense PL observed is owed to the indirect to direct bandgap transition at the K point in the Brillouin zone in monolayers and is severely suppressed in multilayers of MoS₂.⁴⁰ The strong PL response can only be observed for crystalline monolayers and is absent in fully oxidized or bulk regions. The reader should note that the PL is an exceptionally powerful tool which can distinguish monolayer TMDs from their bulk counterpart without any ambiguity. Further, the Raman spectra of MoS₂ flakes in Figure 1h show that the separation between the E_{2g} and A_{1g} peaks of MoS_2 flakes decreased from 25.3 to 21.5 cm⁻¹, which is another clear indication of monolayer survival.41 Finally, the transmission electron microscope (TEM) image of the as-prepared MoS₂ winkled edge shown in Figure 1i indicates the monolayer feature of the flake. The inset corresponds to the selected area electron diffraction (SAED) pattern which reveals excellent crystallinity of the remnant monolayer MoS2 with a hexagonal structure. The annular dark field scanning TEM (ADF-STEM) image in Figure 1j displays the atomic structure of the monolayer MoS2 flake. Mo and S atoms can be identified in the monolayer by analyzing the intensity profile (red dashed-line) due to the Z-contrast (atomic number) characteristics of the ADF-STEM image. In addition, sulfur monovacancies with half the intensity are also observed in the MoS₂ lattice. ⁴² The lattice is intact with minimal defects or distortion after the electrochemical process. The extensive characterization of the remnant MoS₂ flakes unequivocally indicates monolayer formation during the EA process and also confirms the superior chemical stability of the monolayers in oxidative corrosive environments.

Figure 2 demonstrates the EA process for MoS_2 in 0.1 M solutions of HCl, H_2SO_4 , and HNO_3 where multilayer flakes are converted to stable monolayers. Regardless of the electrolyte used in the EA process, the resultant monolayers show similar PL intensity. The PL map colors correspond to the integrated PL peak area with the same range used for all the electrolytes. This indicates that the monolayer formation and subsequent stability of the monolayers are independent of the anionic and cationic species present in the electrolyte. As discussed later, PL intensity can be correlated to the defect density in the basal plane.

Although all these materials have been shown to stabilize monolayers of MoS_2 in highly oxidizing environments, this work focused primarily on TiN. TiN provided a strong interaction stabilizing the monolayers during rapid ablation of the bulk material, was conductive permitting electrooxidation experiments using a traditional electrochemical cell, and did not undergo rapid oxidation and dissolution such as Au did. It also did not catalyze O_2 and H_2 evolution reactions as readily as Pt allowing a wide range of electric potentials to be studied. However, we found that the electrooxidation resistance of the monolayers is not restricted to the TiN. Many conductive

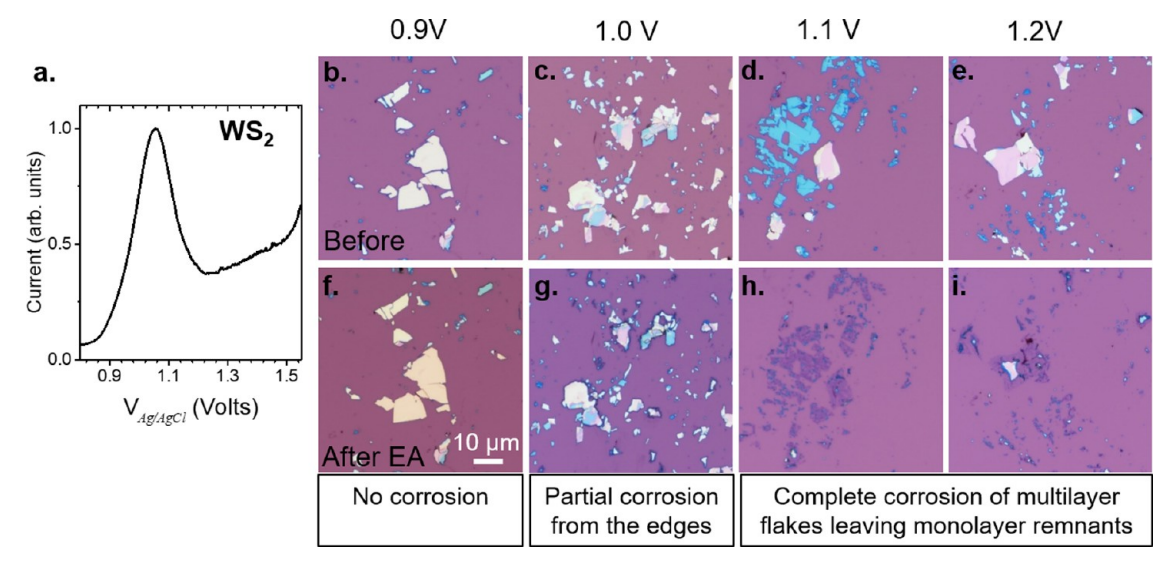


Figure 4. Electrooxidation resistance of WS_2 monolayers. (a) Voltammogram of WS_2 at pH 6 in 1 M LiCl. (b—e) Optical images of WS_2 flakes prior to EA treatment and (f—i) optical images after EA treatment for 60 s at pH 6 at 0.9, 1.0, 1.1, and 1.2 V. Note that monolayers survive even under a positive electrode potential of 1.1 V or greater, corresponding to the position of the voltammogram oxidation peak which corrodes the bulk (multilayer) WS_2 .

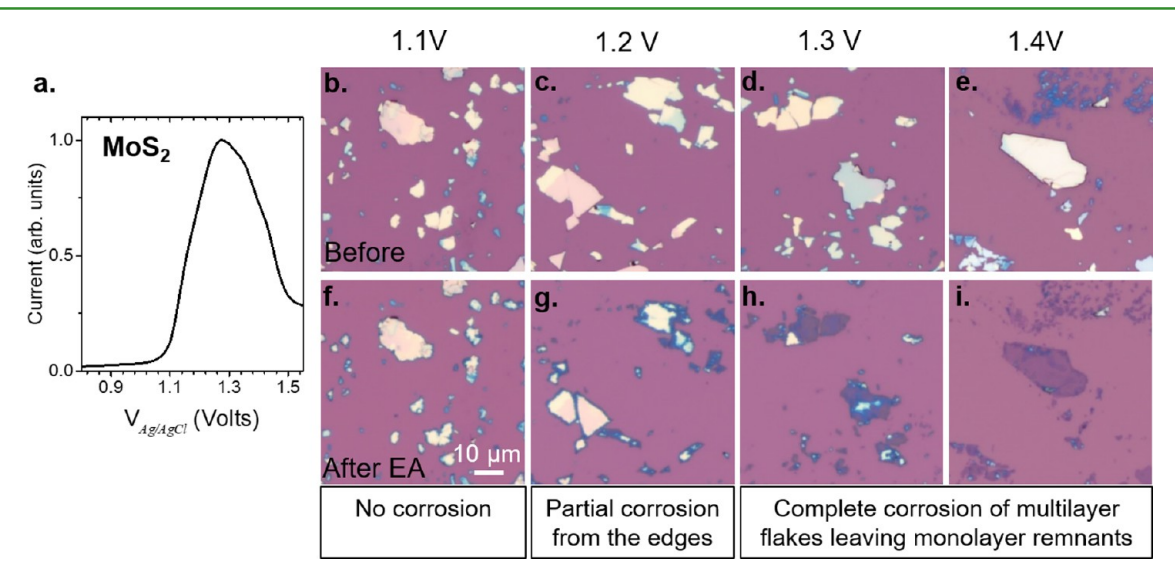


Figure 5. Electrooxidation resistance of MoS_2 monolayers. (a) Voltammogram of MoS_2 at pH 1 in 1 M LiCl. (b—e) Optical images of MoS_2 flakes prior to EA treatment and (f—i) optical images after EA treatment for 60 s at pH 1 at 1.1, 1.2, 1.3, and 1.4 V. Note that monolayers survive even under strong a positive electrode potential of 1.3 V or greater, corresponding to the position of the voltammogram oxidation peak which corrodes the bulk (multilayer) MoS_2 .

substrates such as Au are aggressively oxidized and undergo dissolution at low positive electrode potentials, obscuring the TMD electroablation reactions. 43 On the other hand, more inert substrates such as Pt show results similar to TiN as seen by the optical image and PL map in Figures 3a and 3b. The AFM and line scans are shown in Figures 3c and 3d. Although the step height is ~5 nm and is larger than is shown in Figure 1f on TiN, this is consistent with sample-to-sample variation seen on TiN. The EA process has also been observed on MoS2 flakes extending onto polymer covered regions of the TiN substrate as shown by the optical images in Figures 3e and 3f, confirming the topographic invariance of the EA process. The samples were first prepared by patterning ~60 nm thick PMGI photoresist squares (\sim 2–5 μ m) on the TiN substrate followed by mechanical exfoliation of the MoS₂. Regions of the monolayer MoS2 flake are seen extending on top of the

polymer squares. The AFM and line scan in Figures 3g and 3h confirm that upon EA treatment the MoS_2 on the polymer region was also ablated and converted to monolayer as shown by the $\sim\!4$ nm step height. A step height of $\sim\!4$ nm was also measured on the TiN, consistent with the characterization shown in Figure 1.

As shown in Figures 4a and 5a, anodic peak currents were observed for WS₂ and MoS₂, respectively, during potentiodynamic measurements as the potential was swept in the positive direction from 0 to 2 V versus the Ag/AgCl reference electrode. These peaks are only observable during the first potentiodynamic scan and are attributed to the irreversible oxidative corrosion and monolayer formation of the mechanically exfoliated WS₂ and MoS₂ flakes on the TiN surface (Supporting Information: S3). From Figures 4b to 4i and Figures 5b to 5i, it is obvious that multilayer flakes are readily corroded leaving

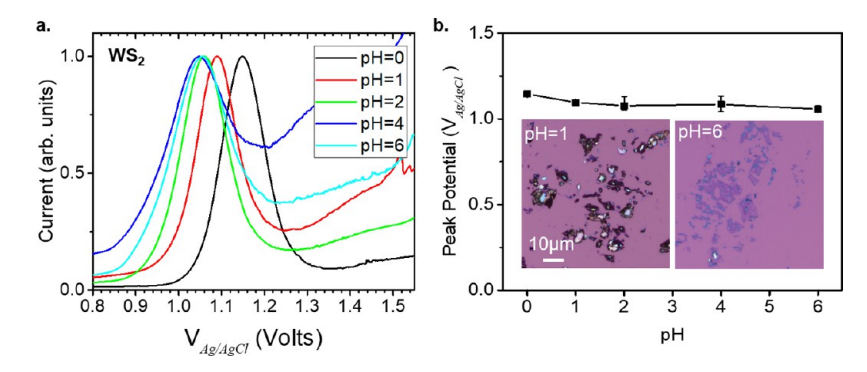


Figure 6. pH dependence of the WS $_2$ EA process. (a) Potentiodynamic voltammogram of mechanically exfoliated WS $_2$ flakes on TiN in 1 M LiCl at different pH conditions. The potential was swept from 0 to 2 V vs Ag/AgCl at a rate of 10 mV/s. The current values have been normalized to account for variations in surface flake density. (b) Plot showing the peak potential position at different pH conditions. A minimum of three measurements were taken at each pH, and the error bars show the minimum and maximum potential extracted. Inset: optical image of WS $_2$ flakes after EA treatment for 60 s at pH 1 (left) with a noticeable black WO $_{3(s)}$ precipitates observed on the surface and at pH 6 (right) where only monolayers and no precipitates are visible.

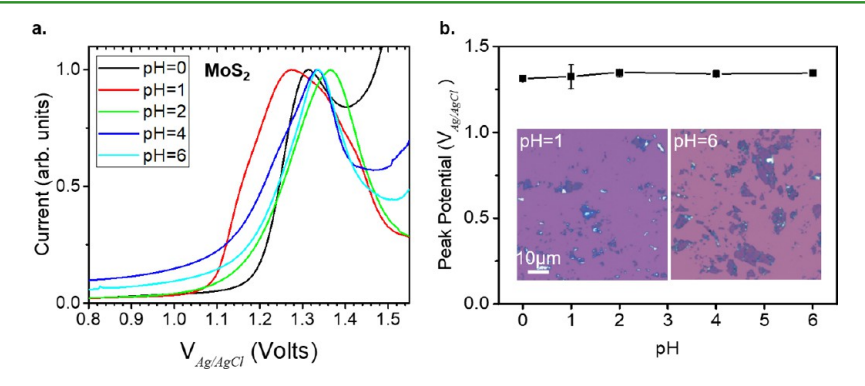


Figure 7. pH dependence of the MoS_2 EA process. (a) Potentiodynamic voltammogram of mechanically exfoliated MoS_2 flakes on TiN in 1 M LiCl at different pH conditions. The potential was swept from 0 to 2 V vs Ag/AgCl at a rate of 10 mV/s. The current values have been normalized to account for variations in surface flake density. (b) Plot showing the peak potential position at different pH conditions. A minimum of three measurements were taken at each pH, and the error bars show the minimum and maximum potential extracted. Inset: optical image of MoS_2 flakes after EA treatment for 60 s at pH 1 (left) and at pH 6 (right). At both acidic and neutral pH conditions only monolayers and no precipitates or residue are visible.

behind the corresponding monolayers when the applied electrode potential is higher than the peak potentials, i.e., 1.06 V for WS₂ at a pH of 6 and 1.3 V for MoS₂ at a pH of 1. At 100 mV below these potentials, limited corrosion occurred at the flake perimeters, and at even lower potentials, no corrosion occurred at all. This verifies that the voltammogram peaks correspond to the WS2 and MoS2 dissolution and that the monolayers are more stable at overpotentials which readily corrodes multilayer flakes. Others have reported analogous cyclic voltammograms with similar peak positions for WS2 and MoS₂ using liquid phase exfoliation where the TMD materials underwent dissolution.^{30,44} At potentials where these peaks occur, the reaction products in acidic conditions, HMoO₄-, WO₄²⁻, and SO₄²⁻, and under more basic conditions, MoO₄²⁻, $WO_{3(s)}$, and SO_4 , are stable in the aqueous phase with the exception of $WO_{3(s)}^{\ \ 45}$ Although this corrosion process readily occurs within seconds, the self-limiting nature leaving monolayers on the substrate is attributed to the strong covalent interaction between the TMDs and the TiN substrate compared to the relatively weak interlayer van der Waals interactions of the bulk materials.³²

The pH dependence of the electroablation oxidation peak is shown in Figures 6 and 7 for WS_2 and MoS_2 , respectively. The anodic peak currents at a pH of 1 occurred at 1.1 and 1.3 V vs Ag/AgCl for WS_2 and MoS_2 , respectively. Since the chalcogen

component, S, is the same for both compounds, their unique electrochemical response is due to the transition metal, Mo and W. It is expected that the WS₂ oxidation peak would occur at a lower potential than for MoS₂ since WS₂ readily oxidizes at 300 °C, whereas MoS₂ oxidizes above 400 °C. Moreover the formation energy of the Mo oxide from its sulfide is 15 kcal/ mol higher than the formation energy of the W oxide from its sulfide. 46 Also, for both bulk materials, the oxidation occurs from the edge planes which is consistent with the edge-tocenter etching observed during the EA process. 46 This is in contrast to what has been reported for MoSe2 where the inert basal plane and uniform edge ablation is only observed for low pH conditions, pH = 1. At higher pH conditions, pH = 2, the flakes ablate from the edges into a pyramidal structure, and at even higher pH conditions, pH > 2, the monolayers are unstable. 47 Under no conditions were WSe2 monolayers found to be stable. Hence, the electrooxidation stability is unique to the disulfides with an electroablation mechanism differing from those found for the diselenides.

 WS_2 shows a decrease in peak potential with increasing pH between a pH of 0 and 2. Interestingly, the potential dependence is negligible for pH values between 2 and 6 with a near zero Nernst slope pointing toward a proton-independent redox couple. Many redox couples exhibit a strong pH dependence reflected via the finite slope of the potential vs

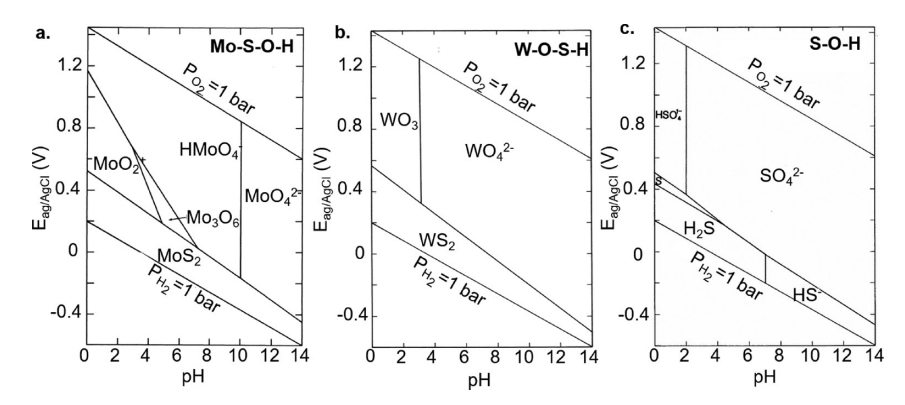


Figure 8. Pourbaix diagrams at 25 °C and 1 bar for the (a) Mo–S–O–H, (b) W–S–O–H, and (c) S–O–H systems. Mo (W) and S activities are 10^{-8} and 10^{-3} , respectively. The potential, $E_{Ag/AgCl}$ is in reference to the Ag/AgCl reference electrode (+0.197 V vs standard hydrogen electrode). Adapted from ref 45. Copyright 1988 Springer-Verlag.

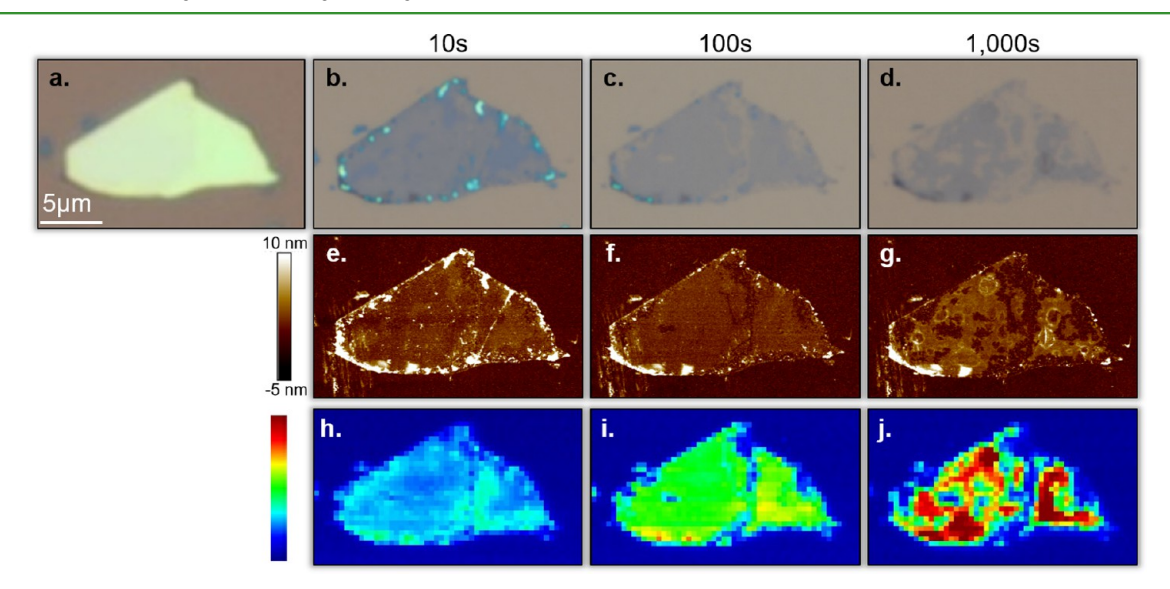


Figure 9. Temporal electrooxidation stability of monolayer MoS_2 . (a) Optical images of a MoS_2 flake before and (b-d) after EA treatment at pH 3 and 1.5 V for 10, 100, and 1000 s, respectively. After 10 and 100 s, most of the monolayer is intact. Only after 1000 s the monolayer begins to visibly oxidize, not from the edges but from random defect sites. This is observed in both the (e-g) AFM and (h-j) PL maps. Upon subsequent treatments, the PL intensity increases due to an increase in sulfur vacancy concentration.

pH plot. This slope is a measure of the ratio of protons to electrons involved according to the Nernst equation. MoS2 also shows a weak but opposite pH dependence from a pH of 0 to 2. This increase in potential is counter to other reports which showed a negative slope in the 0-8 pH range of approximately 30 mV/pH which, according to the Nernst equation, corresponds to a Mo4+ to Mo6+ two-electron, one-proton transfer process.³⁰ However, a closer inspection of the MoS₂ voltammograms, in particular at a pH of 4 and 6, reveals an asymmetrical peak with a lower intensity shoulder at slightly lower potentials. This could be attributed to two oxidation peaks: one corresponding to oxidation from the edges and another at a lower potential corresponding to oxidation from the basal plane. Kautek and Gerischer identified two oxidation peaks in bulk MoS2 with a separation of ~0.18 V, similar to what is observed in the MoS₂ voltammograms.⁴⁸ Factors such as the exfoliated flake size and hence the edge-to-basal plane ratios between samples could contribute to variations in the two oxidation peak intensities. Basal and edge overlapping peaks would explain the variation in peak shape observed and obfuscate the true reaction pH dependence. While some have attempted to study the pH dependence on TMD oxidation

with varying success, precise reproducible measurements are difficult. The irreversible nature of the corrosion process coupled with complicated reaction pathways and/or measurement factors such as scan rate, electrode geometry, relative electrode, and mass transport rates are accountable for the pHdependent behavior. 49 From viewing the Mo-O-S and W-O-S Pourbaix diagrams in Figure 8, it is apparent that different reaction products are observed at different pH and potential ranges which could give rise to the relatively pH-independent behavior observed for both MoS₂ and WS₂. 45 It is also unknown how the TiN substrate affects the reaction pathways or catalyzes these oxidation reactions. In the case of WS₂, upon inspection of the EA formed monolayers and as predicted by the Pourbaix diagrams, it is immediately apparent that at low pH conditions the W oxidation product is insoluble $WO_{3(s)}$, as evident by the black or multicolored residue left after the EA treatment shown in Figure 6. In contrast, at pH conditions between 0 and 6, all probable Mo oxidation products, MoO2+, HMoO₄⁻, and MoO₄²⁻, are water/aqueous soluble and hence leave pristine looking monolayers at all the pH values tested. However, at a pH of 6, the stable W oxidation product is now aqueous $WO_4^{\ 2-}$, and no visible solid oxide residue is observed. The WS₂ monolayers are visually similar to those of MoS₂ with no observable precipitates. Therefore, if the intent is to achieve WS2 and other W containing TMD monolayers by means of an EA process, it must be done under conditions which result in soluble oxidized species, a limitation not observed for MoS₂.

Finally, electrooxidation stability of monolayer flakes was investigated for EA treatments up to 100 and 1000 s for WS2 and MoS₂, respectively. As shown in Figure 9, a multilayer MoS₂ flake (Figure 9a) is rapidly ablated down to monolayer (Figure 9b) within 10 s when a positive potential of 1.5 V is applied under a pH of 3, which is confirmed by the AFM image (Figure 9e) and the PL map (Figure 9h). However, when the EA process is continued for a longer duration of time beyond the formation of monolayer MoS2, visible changes start to appear. For example, after 100 s, the monolayer region begins to undergo dissolution which becomes more pronounced after 1000 s. The optical and AFM images in Figures 9c,d and 9f,g, respectively, confirm the delayed corrosion and hence superior electrooxidation resistance of MoS₂ monolayers compared to its bulk counterpart. It is interesting to note that the electrooxidation leading to the dissolution of the monolayer does not initiate at the edges as does the ablation of the multilayer flakes but nucleates randomly across the sample. Moreover, Figures 9h-j clearly show a monotonic increase in the PL intensity of the monolayer MoS₂ as the electrooxidation process continues. While PL intensity is usually thought to increase with improved crystal quality, it can also be due to defect sites interacting with adsorbed gas species. 50 We believe that the electrooxidation process introduces sulfur vacancies which enhances the PL, and at the same time these sulfur vacancies serve as nucleation site for the monolayer etching while the edges still remain resistant to oxidation. In Figure 10, it is seen that WS2 undergoes a similar type of monolayer etching, however much more severe and after only 100 s. The AFM shows that the WS2 oxidation products do not have sufficient time to dissolve before

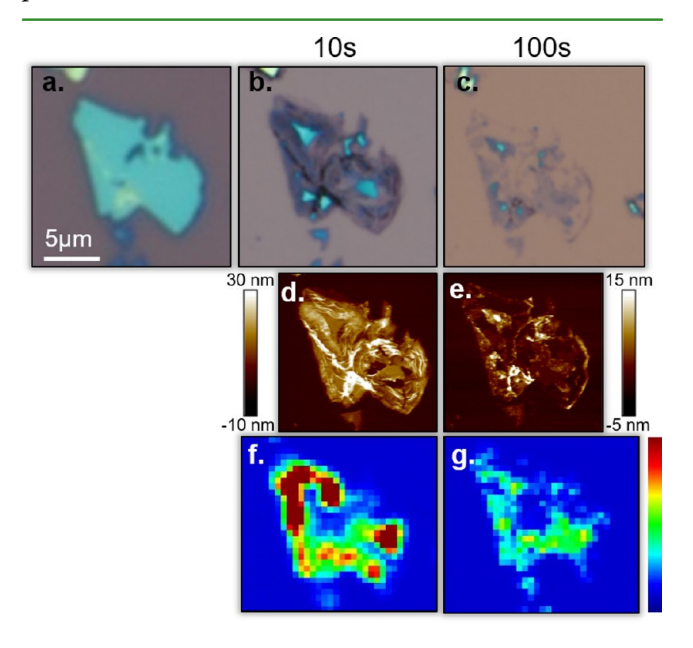


Figure 10. Temporal electrooxidation stability of monolayer WS₂. (a) Optical images of a WS2 flake before and (b, c) after EA treatment at pH 6 and 1.1 V for 10 and 100 s, respectively. After 10 s the monolayer is intact. Only after 100 s the monolayer begins to visibly oxidize, not from the edges but from random defect sites. This is observed in both the (d, e) AFM and (f, g) PL maps.

significant monolayer etching occurs. In contrast to MoS₂ further EA treatment does not increase the PL intensity of WS₂. The more rapid etching of WS₂ arises due to how oxygen species interact with the electrochemically created S vacancies in MoS₂ and WS₂. It is interesting to note that S vacancies have a higher energy of formation in WS₂ compared to MoS₂, 2.856 and 2.681 eV, respectively. However, the adsorption energy of an O2 molecule on these S vacancy is 1.843 eV vs 2.082 eV for MoS₂ and WS₂, indicating a weaker oxygen-vacancy interaction for MoS₂. Further MoS₂ has a larger energy barrier, 0.93 eV vs 0.86 eV, for O dissociation and thus less susceptible to oxidation at the vacancy site.⁵¹

CONCLUSION AND SUMMARY

In summary, exceptional corrosion resistance and superior electrooxidation stability of monolayer WS2 and MoS2 on TiN has been demonstrated and extensively characterized. The layered van der Waals structure of these materials permits a strong monolayer/substrate interaction which deactivates the highly reactive edge sites responsible for the oxidation and corrosion of the multilayer regions. Our results indicate that the TMD class of materials, particularly the disulfides, shows great promise and potential economic impact for atomically thin anticorrosion applications and similarly suggest high stability and longevity where TMDs are used as active device components. The electrochemical voltammograms displayed a well-defined anodic peak current responsible for the TMD oxidation and dissolution. Upon EA treatment, a visible contrast difference, Raman spectroscopy, PL map, AFM, and HRTEM confirmed that monolayer remnants remain at high over potentials which readily oxidized the multilayer flakes. A relatively pH independence near zero Nernst slope was observed, and reaction products were hypothesized. In particular, it was experimentally confirmed that WS₂ produces insoluble WO_{3(s)} precipitates in acidic conditions while the products are soluble in neutral conditions. In contrast, MoS₂ products were soluble in the entire pH range tested leaving pristine monolayer films. However, the voltammograms suggest two oxidation processes occurred which are believed to correspond to basal plane and edge oxidation. While both MoS₂ and WS₂ monolayers eventually begin to undergo dissolution owing to electrooxidation, the rate is orders of magnitude slower than the ablation of the multilayers. Further, the process appears to be catalyzed by defects, not by edge site reactivity.

■ EXPERIMENTAL METHODS

Sample Preparation and Materials. West Coast Silicon provided 0.01-0.02 ohm·cm 4 in. Si wafers with 100 nm of sputtered TiN. Immediately prior to sample preparation, TiN substrates were treated in an Allwin21 Heatpulse 610 rapid thermal processing tool at 500 °C for 10 min under N₂ ambient. The use of TiN as the substrate was motivated by its superior stability under severe positive electrode potentials and oxidation conditions which allows us to study the unique corrosion chemistry of the TMDs. Pt substrates were prepared by sputtering 100 nm of Pt onto a Si wafer. MoS2 and WS2 crystals obtained from 2D Semiconductors were mechanically exfoliated onto \sim 15 mm \times 15 mm substrates. Please note that mechanical exfoliation provides pristine quality single crystalline material and at the same time allows to repeat hundreds of experiments. However, mechanical exfoliation is not scalable, and therefore practical implementation of TMD materials as anticorrosion coating would necessitate large area growth of monolayer materials. In this context, we would like to point out that significant progress has been made in recent times in chemical

vapor deposition (CVD) growth of TMD monolayers over areas as large as cm 2 . A Solartron Analytical 1287 potentiostat in conjunction with a 6 mm Ag/AgCl reference electrode supplied by BASi and a Graftech Grafoil auxiliary electrode were used for electrochemical experiments. The 1 M LiCl electrolyte solution was prepared with LiCl salt supplied by VWR and deionized water. The pH was balanced using HCl and measured using a Mettler Toledo SevenMulti pH meter. Acid electrolyte solutions were prepared by diluting concentrated HNO3, $\rm H_2SO_4$, and HCl.

Electrochemical Measurements and Characterization. An electrochemical cell setup using ~25 mL of electrolyte solution similar to previously reported work was used.³² The sample was suspended from a metal clip with ~25 mm² immersed into the electrolyte solution. Potentiodynamic measurements were made by sweeping from 0 to 2 V vs the Ag/AgCl reference electrode at a scan rate of 10 mV/s. A minimum of three potentiodynamic measurements were taken at each pH. Potentiostatic etching treatments were performed by applying a fixed potential. Raman and photoluminescence measurements were made using a Horiba LabRAM HR Evolution spectrometer and a laser excitation wavelength of 488 and 532 nm. AFM measurements were made using a Bruker Dimension Icon. The as-prepared MoS2 was transferred from the TiN substrate to a Quantifoil Au TEM grid by a PMMA-assisted method.⁵² transmission electron microscope, a FEI Titan³ (60-300) at 80 kV at Penn State University, was used to examine and study the atomic and chemical structure of the MoS₂.

■ ASSOCIATED CONTENT

Supporting Information

The Supporting Information is available free of charge on the ACS Publications website at DOI: 10.1021/acsami.7b17660.

Cyclic voltammograms for MoS₂ and WS₂ showing two complete cycles; Raman spectra of WS₂ before and after EA (PDF)

AUTHOR INFORMATION

Corresponding Author

*E-mail sud70@psu.edu, das.sapt@gmail.com (S.D.).

ORCID

Daniel S. Schulman: 0000-0002-0751-0578 Saptarshi Das: 0000-0002-0188-945X

Notes

The authors declare no competing financial interest.

ACKNOWLEDGMENTS

The work of D.S.S. and S.D. was partially supported through Grant ECCS-1640020 from National Science Foundation (NSF) and Contract 2016-NE-2699 from Nanoelectronic Research Corporation. The work of F.Z. and N.A. was partially supported from the National Science Foundation under EFRI 2-DARE awards 1433378.

REFERENCES

- (1) Bewilogua, K.; Hofmann, D. History of diamond-like carbon films From first experiments to worldwide applications. *Surf. Coat. Technol.* **2014**, 242, 214–225.
- (2) Montemor, M. F. Functional and smart coatings for corrosion protection: A review of recent advances. *Surf. Coat. Technol.* **2014**, 258, 17–37.
- (3) Singh, B. P.; Jena, B. K.; Bhattacharjee, S.; Besra, L. Development of oxidation and corrosion resistance hydrophobic graphene oxide-polymer composite coating on copper. *Surf. Coat. Technol.* **2013**, 232, 475–481.

- (4) Novoselov, K. S.; Geim, A. K.; Morozov, S. V.; Jiang, D.; Zhang, Y.; Dubonos, S. V.; Grigorieva, I. V.; Firsov, A. A. Electric field effect in atomically thin carbon films. *Science* **2004**, *306*, 666–9.
- (5) Wang, Q. J.; Chung, Y. Encyclopedia of Tribology; Springer: New York, 2013.
- (6) Hu, X. G.; Jiang, P.; Wan, J. C.; Xu, Y. F.; Sun, X. J. Study of corrosion and friction reduction of electroless Ni-P coating with molybdenum disulfide nanoparticles. *J. Coat. Technol. Res.* **2009**, *6*, 275–281.
- (7) Rossi, S.; Chini, F.; Straffelini, G.; Bonora, P. L.; Moschini, R.; Stampali, A. Corrosion protection properties of electroless Nickel/ PTFE, Phosphate/MoS $_2$ and Bronze/PTFE coatings applied to improve the wear resistance of carbon steel. *Surf. Coat. Technol.* **2003**, *173*, 235–242.
- (8) Li, H.; Tsai, C.; Koh, A. L.; Cai, L.; Contryman, A. W.; Fragapane, A. H.; Zhao, J.; Han, H. S.; Manoharan, H. C.; Abild-Pedersen, F.; Norskov, J. K.; Zheng, X. Activating and optimizing MoS2 basal planes for hydrogen evolution through the formation of strained sulphur vacancies. *Nat. Mater.* **2016**, *15*, 48–53.
- (9) Lukowski, M. A.; Daniel, A. S.; Meng, F.; Forticaux, A.; Li, L.; Jin, S. Enhanced hydrogen evolution catalysis from chemically exfoliated metallic MoS₂ nanosheets. *J. Am. Chem. Soc.* **2013**, *135*, 10274–7.
- (10) Voiry, D.; Salehi, M.; Silva, R.; Fujita, T.; Chen, M.; Asefa, T.; Shenoy, V. B.; Eda, G.; Chhowalla, M. Conducting MoS₂ nanosheets as catalysts for hydrogen evolution reaction. *Nano Lett.* **2013**, *13*, 6222–7
- (11) Kline, G.; Kam, K.; Canfield, D.; Parkinson, B. A. Efficient and Stable Photoelectrochemical Cells Constructed with WSe₂ and MoSe₂ Photoanodes. *Sol. Energy Mater.* **1981**, *4*, 301–308.
- (12) Kline, G.; Kam, K. K.; Ziegler, R.; Parkinson, B. A. Further studies of the photoelectrochemical properties of the group VI transition metal dichalcogenides. *Sol. Energy Mater.* **1982**, *6*, 337–350.
- (13) Whittingham, M. S.; Dines, M. B. Surv. Prog. Chem. **1980**, 9, 55–87.
- (14) Savjani, N.; Lewis, E. A.; Bissett, M. A.; Brent, J. R.; Dryfe, R. A. W.; Haigh, S. J.; O'Brien, P. Synthesis of Lateral Size-Controlled Monolayer 1H-MoS₂@Oleylamine as Supercapacitor Electrodes. *Chem. Mater.* **2016**, *28*, 657–664.
- (15) Weng, Q.; Wang, X.; Wang, X.; Zhang, C.; Jiang, X.; Bando, Y.; Golberg, D. Supercapacitive energy storage performance of molybdenum disulfide nanosheets wrapped with microporous carbons. *J. Mater. Chem. A* **2015**, *3*, 3097–3102.
- (16) Mak, K. F.; He, K.; Shan, J.; Heinz, T. F. Control of valley polarization in monolayer MoS₂ by optical helicity. *Nat. Nanotechnol.* **2012**, *7*, 494–8.
- (17) Ross, J. S.; Klement, P.; Jones, A. M.; Ghimire, N. J.; Yan, J.; Mandrus, D. G.; Taniguchi, T.; Watanabe, K.; Kitamura, K.; Yao, W.; Cobden, D. H.; Xu, X. Electrically tunable excitonic light-emitting diodes based on monolayer WSe₂ p—n junctions. *Nat. Nanotechnol.* **2014**, *9*, 268–72.
- (18) Wu, W.; Wang, L.; Li, Y.; Zhang, F.; Lin, L.; Niu, S.; Chenet, D.; Zhang, X.; Hao, Y.; Heinz, T. F.; Hone, J.; Wang, Z. L. Piezoelectricity of single-atomic-layer MoS_2 for energy conversion and piezotronics. *Nature* **2014**, *514*, 470–4.
- (19) Kumar, A.; Ahluwalia, P. Semiconductor to metal transition in bilayer transition metals dichalcogenides MX_2 (M = Mo, W; X = S, Se, Te). *Modell. Simul. Mater. Sci. Eng.* **2013**, *21*, 065015.
- (20) Wang, L.; Wang, Y.; Wong, J. I.; Palacios, T.; Kong, J.; Yang, H. Y. Functionalized MoS₂ nanosheet-based field-effect biosensor for label-free sensitive detection of cancer marker proteins in solution. *Small* **2014**, *10*, 1101–5.
- (21) van der Zande, A. M.; Barton, R. A.; Alden, J. S.; Ruiz-Vargas, C. S.; Whitney, W. S.; Pham, P. H.; Park, J.; Parpia, J. M.; Craighead, H. G.; McEuen, P. L. Large-scale arrays of single-layer graphene resonators. *Nano Lett.* **2010**, *10*, 4869–4873.
- (22) Yang, J.; Wang, Z.; Wang, F.; Xu, R. J.; Tao, J.; Zhang, S.; Qin, Q. H.; Luther-Davies, B.; Jagadish, C.; Yu, Z. F.; Lu, Y. R. Atomically thin optical lenses and gratings. *Light: Sci. Appl.* **2016**, *5*, e16046.

- (23) Liu, L. H.; Xu, K.; Wan, X.; Xu, J. B.; Wong, C. Y.; Tsang, H. K. Enhanced optical Kerr nonlinearity of MoS₂ on silicon waveguides. *Photonics Res.* **2015**, *3*, 206–209.
- (24) Tan, Y.; He, R.; Cheng, C.; Wang, D.; Chen, Y.; Chen, F. Polarization-dependent optical absorption of MoS₂ for refractive index sensing. *Sci. Rep.* **2015**, *4*, 7523.
- (25) Schulman, D. S.; Sebastian, A.; Buzzell, D.; Huang, Y. T.; Arnold, A. J.; Das, S. Facile Electrochemical Synthesis of 2D Monolayers for High Performance Thin Film Transistors. *ACS Appl. Mater. Interfaces* **2017**, *9*, 44617.
- (26) Jaegermann, W.; Schmeisser, D. Reactivity of Layer Type Transition-Metal Chalcogenides Towards Oxidation. *Surf. Sci.* **1986**, *165*, 143–160.
- (27) Suzuki, K.; Soma, M.; Onishi, T.; Tamaru, K. Reactivity of Molybdenum-Disulfide Surfaces Studied by XPS. *J. Electron Spectrosc. Relat. Phenom.* **1981**, *24*, 283–287.
- (28) Ambrosi, A.; Sofer, Z.; Pumera, M. Lithium intercalation compound dramatically influences the electrochemical properties of exfoliated MoS₂. *Small* **2015**, *11*, 605–12.
- (29) Eng, A. Y.; Ambrosi, A.; Sofer, Z.; Simek, P.; Pumera, M. Electrochemistry of transition metal dichalcogenides: strong dependence on the metal-to-chalcogen composition and exfoliation method. *ACS Nano* **2014**, *8*, 12185–98.
- (30) Zafir Mohamad Nasir, M.; Sofer, Z.; Pumera, M. Effect of Electrolyte pH on the Inherent Electrochemistry of Layered Transition-Metal Dichalcogenides (MoS₂, MoSe₂, WSe₂). ChemElectroChem. **2015**, 2, 1713–1718.
- (31) Castellanos-Gomez, A.; Barkelid, M.; Goossens, A. M.; Calado, V. E.; van der Zant, H. S.; Steele, G. A. Laser-thinning of MoS₂: on demand generation of a single-layer semiconductor. *Nano Lett.* **2012**, 12, 3187–92.
- (32) Das, S.; Bera, M. K.; Tong, S.; Narayanan, B.; Kamath, G.; Mane, A.; Paulikas, A. P.; Antonio, M. R.; Sankaranarayanan, S. K.; Roelofs, A. K. A Self-Limiting Electro-Ablation Technique for the Top-Down Synthesis of Large-Area Monolayer Flakes of 2D Materials. *Sci. Rep.* **2016**, *6*, 28195.
- (33) Lu, X.; Utama, M. I.; Zhang, J.; Zhao, Y.; Xiong, Q. Layer-by-layer thinning of MoS₂ by thermal annealing. *Nanoscale* **2013**, 5, 8904—8.
- (34) Xiao, S.; Xiao, P.; Zhang, X.; Yan, D.; Gu, X.; Qin, F.; Ni, Z.; Han, Z. J.; Ostrikov, K. K. Atomic-layer soft plasma etching of MoS₂. *Sci. Rep.* **2016**, *6*, 19945.
- (35) Doganov, R. A.; O'Farrell, E. C.; Koenig, S. P.; Yeo, Y.; Ziletti, A.; Carvalho, A.; Campbell, D. K.; Coker, D. F.; Watanabe, K.; Taniguchi, T.; Castro Neto, A. H.; Ozyilmaz, B. Transport properties of pristine few-layer black phosphorus by van der Waals passivation in an inert atmosphere. *Nat. Commun.* **2015**, *6*, 6647.
- (36) Guo, Y.; Zhou, S.; Bai, Y.; Zhao, J. Oxidation Resistance of Monolayer Group-IV Monochalcogenides. *ACS Appl. Mater. Interfaces* **2017**, *9*, 12013–12020.
- (37) Gomes, L. C.; Carvalho, A.; Neto, A. H. C. Vacancies and oxidation of two-dimensional group-IV monochalcogenides. *Phys. Rev. B: Condens. Matter Mater. Phys.* **2016**, *94*, 054103.
- (38) Tongay, S.; Zhou, J.; Ataca, C.; Liu, J.; Kang, J. S.; Matthews, T. S.; You, L.; Li, J.; Grossman, J. C.; Wu, J. Broad-range modulation of light emission in two-dimensional semiconductors by molecular physisorption gating. *Nano Lett.* **2013**, *13*, 2831–6.
- (39) Liu, H. S.; Han, N. N.; Zhao, J. J. Atomistic insight into the oxidation of monolayer transition metal dichalcogenides: from structures to electronic properties. *RSC Adv.* **2015**, *5*, 17572–17581.
- (40) Das, S.; Robinson, J. A.; Dubey, M.; Terrones, H.; Terrones, M. Beyond Graphene: Progress in Novel Two-Dimensional Materials and van der Waals Solids. *Annu. Rev. Mater. Res.* **2015**, *45*, 1–27.
- (41) Li, H.; Zhang, Q.; Yap, C. C. R.; Tay, B. K.; Edwin, T. H. T.; Olivier, A.; Baillargeat, D. From Bulk to Monolayer MoS₂: Evolution of Raman Scattering. *Adv. Funct. Mater.* **2012**, *22*, 1385–1390.
- (42) Williams, D. B.; Carter, C. B. The Transmission Electron Microscope; Springer: Boston, MA, 1996.

- (43) Cherevko, S.; Topalov, A. A.; Zeradjanin, A. R.; Katsounaros, I.; Mayrhofer, K. J. J. Gold dissolution: towards understanding of noble metal corrosion. *RSC Adv.* **2013**, *3*, 16516–16527.
- (44) Chia, X.; Eng, A. Y.; Ambrosi, A.; Tan, S. M.; Pumera, M. Electrochemistry of Nanostructured Layered Transition-Metal Dichalcogenides. *Chem. Rev.* **2015**, *115*, 11941–66.
- (45) Brookins, D. G. Eh-pH Diagrams for Geochemistry; Springer: Berlin, 1988.
- (46) Miremadi, B. K.; Morrison, S. R. The Intercalation and Exfoliation of Tungsten Disulfide. *J. Appl. Phys.* **1988**, *63*, 4970–4974.
- (47) Huang, Y. T.; Dodda, A.; Schulman, D. S.; Sebastian, A.; Zhang, F.; Buzzell, D.; Terrones, M.; Feng, S. P.; Das, S. Anomalous Corrosion of Bulk Transition Metal Diselenides Leading to Stable Monolayers. ACS Appl. Mater. Interfaces 2017, 9, 39059–39068.
- (48) Kautek, W.; Gerischer, H. Anisotropic photocorrosion of n-type MoS₂, MoSe₂, and WSe₂ single crystal surfaces: the role 0f cleavage steps, line and screw dislocations. *Surf. Sci.* **1982**, *119*, 46–60.
- (49) Brownson, D. A. C.; Banks, C. E. The Handbook of Graphene Electrochemistry, 1st ed.; Springer-Verlag: London, 2014.
- (50) Tongay, S.; Suh, J.; Ataca, C.; Fan, W.; Luce, A.; Kang, J. S.; Liu, J.; Ko, C.; Raghunathanan, R.; Zhou, J.; Ogletree, F.; Li, J.; Grossman, J. C.; Wu, J. Defects activated photoluminescence in two-dimensional semiconductors: interplay between bound, charged, and free excitons. *Sci. Rep.* **2013**, *3*, 2657.
- (51) Liu, H.; Han, N.; Zhao, J. Atomistic insight into the oxidation of monolayer transition metal dichalcogenides: from structures to electronic properties. *RSC Adv.* **2015**, *5*, 17572–17581.
- (52) Zhang, F.; Erb, C.; Runkle, L.; Zhang, X.; Alem, N. Etchant-free Transfer of 2D Nanostructures. *Nanotechnology* **2018**, *29*, 025602.